

High-precision compliant mechanism for lens XY micro-adjustment

Cite as: Rev. Sci. Instrum. **91**, 035004 (2020); <https://doi.org/10.1063/1.5141138>

Submitted: 14 December 2019 . Accepted: 09 March 2020 . Published Online: 24 March 2020

Lei Zhao, Xinfeng Yu, Pengzhi Li, and Yanfeng Qiao



View Online



Export Citation



CrossMark

ARTICLES YOU MAY BE INTERESTED IN

[A novel design of a high-performance flexure hinge with reverse parallel connection multiple-cross-springs](#)

Review of Scientific Instruments **91**, 035121 (2020); <https://doi.org/10.1063/1.5096878>

[Design and stiffness modeling of a four-degree-of-freedom nanopositioning stage based on six-branched-chain compliant parallel mechanisms](#)

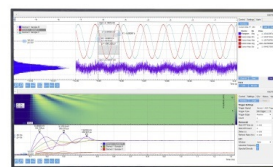
Review of Scientific Instruments **91**, 065002 (2020); <https://doi.org/10.1063/5.0008905>

[Resonant-type piezoelectric linear motor driven by harmonic synthesized mechanical square wave](#)

Review of Scientific Instruments **91**, 035005 (2020); <https://doi.org/10.1063/1.5110774>

Challenge us.

What are your needs for periodic signal detection?



Zurich
Instruments



High-precision compliant mechanism for lens XY micro-adjustment

Cite as: Rev. Sci. Instrum. 91, 035004 (2020); doi: 10.1063/1.5141138

Submitted: 14 December 2019 • Accepted: 9 March 2020 •

Published Online: 24 March 2020



View Online



Export Citation



CrossMark

Lei Zhao,^{1,a)} Xinfeng Yu,^{1,2,b)} Pengzhi Li,^{3,b)} and Yanfeng Qiao^{1,b)}

AFFILIATIONS

¹Changchun Institute of Optics, Fine Mechanics and Physics, Chinese Academy of Sciences, Dongnanhu Road, 3888#, 130033 Changchun, People's Republic of China

²University of Chinese Academy of Sciences, Yuquan Road, 19#A, 100049 Beijing, People's Republic of China

³Robotics for Extreme Environments Lab (REEL), School of Electrical and Electronic Engineering, The University of Manchester, Manchester M139PL, United Kingdom

^{a)} Author to whom correspondence should be addressed: zhaolei1218@126.com. Tel.: +86 43186708012. Fax: +86 43186708255

^{b)} Electronic addresses: yu_xfeng@126.com; pengzhi.li@manchester.ac.uk; and qiaoyf@ciomp.ac.cn

ABSTRACT

The high resolution of lithography lenses has led to a requirement for high-precision lens-adjusting compensators. This paper presents the design, analysis, and testing of a high-precision two-degrees-of-freedom compliant mechanism to be used for lens XY micro-adjustment. The monolithic mechanism, which is based on a 1RR–2RRR configuration, uses flexure hinges to connect the movable inner ring with the fixed outer ring. The apparatus is driven using two piezoelectric actuators, and the lens terminal displacement is fed back in real time using two capacitive sensors. This paper describes the principle of the mechanism. Simulations and experiments are then performed to evaluate the system. The results show that the strokes along both the x -axis and the y -axis exceed $\pm 25 \mu\text{m}$. The accuracy of the proposed mechanism is better than $\pm 7 \text{ nm}$. The root-mean-square induced figure error is better than 0.051 nm . The coupling z and tip/tilt rigid motions are less than 50 nm and 220 mas , respectively. The first natural frequency of the mechanism is 212 Hz . These results indicate that the mechanism has advantages that include high accuracy, low coupling errors, high rigidity, and compactness and that it will act as an efficient compensator for lithography lenses.

Published under license by AIP Publishing. <https://doi.org/10.1063/1.5141138>

I. INTRODUCTION

A compliant mechanism is typically a monolithic structure that uses flexure hinges rather than classical rotation joints to connect a fixed part to a movable part and, thus, transfer motion, force, and energy between the two parts. A compliant mechanism that is based on flexure hinges offers several advantages, including zero friction losses, no lubrication requirements, zero hysteresis, a compact structure, a capacity for use in small-scale applications, ease of fabrication, and virtually no assembly or maintenance requirements.¹ Compliant mechanisms have been incorporated into a wide variety of applications, including translation micropositioning stages,^{2–5} fast-tool-servo diamond turning equipment,^{6–9} high-accuracy alignment devices for optical systems,^{10–15} imprint lithography systems,¹⁶ and many other leading technologies. Polit and Dong, for example, presented an XY stage that was composed of

a doubly clamped beam and a parallelogram-shaped hybrid flexure with compliant beams and a circular flexure hinge. The travel range of this stage exceeded $15 \mu\text{m}$, its resolution was 1 nm , its first frequency exceeded 8 kHz , and its closed-loop bandwidth was 2 kHz , but the stage uses a parallelogram mechanism to enlarge the size, and the end effector is not uniformly supported, so out-of-plane coupling errors are hard to control.⁴ Rakuff and Cuttino introduced a long-range, high-precision fast-tool-servo flexure mechanism for a diamond turning machine in which the system was driven using a voice coil actuator, a custom linear current amplifier, and a laser interferometer feedback system. The maximum acceleration of their system was 260 m/s^2 , its bandwidth ranged up to 140 Hz , and its maximum displacement range was 2 mm , but it is only one-degree-of-freedom (DOF), and there is no tough requirement of space dimensions.⁷ Ajit *et al.* designed a flexure lens focusing motion stage with a stroke range of $\pm 0.7 \text{ mm}$ in less than 14 ms , but the

stage is used to move only along the z axis and it has adequate space.¹⁰

In the lithography field, lithography lenses with increasingly high resolution are required because the critical dimensions of gigascale integrated circuits are becoming extremely small.¹⁷ Several movable lenses that are components in lithographic lenses are used during the lens assembly and working processes to improve lithographic performance by compensating for focus, distortion, astigmatism, coma, and other aberrations. These mechanisms require nanometer-scale accuracy, real-time responses, and low coupling errors, and as a cell needs to be installed into a projection lens with dozens of lenses, it must be highly compact.^{18–21}

To meet the above-mentioned requirements for the lens adjustment mechanism, this paper presents a monolithic compliant mechanism for lens XY micro-adjustment. The mechanism based on 1RR–2RRR configuration uses two actuators to achieve XY two-degree-of-freedom movement. This article uses the pseudo-rigid-body model to calculate the Jacobi matrix and then uses FEM and experiment methods to confirm the results. The remainder of the paper is organized as follows: Section II introduces the principle of the mechanism, which is based on the pseudo-rigid-body method. Section III presents the frame structure of the mechanism. Sections IV and V present the simulation results and the experimental results, respectively. Conclusions are presented in Sec. VI.

II. PRINCIPLE OF THE XY COMPLIANT MECHANISM

The XY compliant mechanism uses a 1RR–2RRR configuration. The mechanism has eight rotation joints and five straight rods. The 1RR part on the top contains two rotation joints (D_1 , E_1) and one straight rod (D_1E_1) and provides one passive constraint in the D_1E_1 direction. The left 2RRR part contains three rotation joints (A_1 , B_1 , C_1) and two straight rods (A_1B_1 , B_1C_1) and provides one actuated constraint along the B_1C_1 direction. The right 2RRR part contains three rotation joints (A_2 , B_2 , C_2) and two straight rods (A_2B_2 , B_2C_2) and provides one more actuated constraint along the B_2C_2 direction. The degree-of-freedom (DOF) of the 1RR–2RRR parallel mechanism can be calculated as

$$DOF = 3n - (2p_l + p_h), \quad (1)$$

where n is the number of active components in the mechanism, p_l is the number of lower planar joints in the mechanism, and p_h is the number of higher planar joints in the mechanism. For the proposed

1RR–2RRR parallel mechanism, n is 6 (based on one end effector and five rigid linkages), while p_l is 8 (based on eight planar rotation joints), and p_h is 0; the DOF of the mechanism is therefore 2, and two input forces/displacements are required.

The constraint lines D_1E_1 and B_2C_2 form the instant center O_1 , while the constraint lines D_1E_1 and B_1C_1 form the instant center O_2 . B_1C_1 and B_2C_2 are arranged nearly tangent to the circular to reduce x - y coupling. Therefore, when an input displacement/force actuates rod A_1B_1 , the lens moves approximately in the x -direction, as shown in Fig. 1(a). In contrast, when the input displacement/force actuates rod A_2B_2 , the lens then moves approximately in the y direction, as shown in Fig. 1(b).

III. GENERAL FRAME OF THE XY COMPLIANT MECHANISM

Figure 2 shows the general frame for the proposed XY mechanism system. The system comprises the XY mechanism, a supporting cell, two piezomotors, two position sensors, and two leaf springs. The lens is glued onto the supporting cell, and the two components are then connected to the XY compliant mechanism using several screws. The XY compliant mechanism is a monolithic structure with an inner ring and an outer ring, which are connected through a top single flexure, left and right folded-hinge flexures, and several L-shaped flexures. The top single flexure is an RR structure, while the folded-hinge flexures are RRR structures, and thus, the single flexure and the two folded-hinge flexures form the 1RR–2RRR configuration. The L-shaped flexures are used to balance the weight of the moving part of the mechanism. The XY compliant mechanism can be manufactured using a low-speed wire electrical-discharge-machining. The two piezomotors are assembled on the outer ring of the XY compliant mechanism, and the force/displacement of each piezomotor's moving head is applied to the outer linkage of the folded-hinge flexure. In the direction opposite to that of the piezomotor, a leaf spring is applied to the linkage to preload the mechanism. Two capacitive displacement sensors are then assembled on the outer ring of the XY compliant mechanism to measure the movement of the inner part. The circumference angle between the two displacement sensors is approximately 90° . The mechanism connects other lens sub-houses through threaded connection, which are equally spaced on the outer ring, and as a sub-house, it will be permanently left inside the lithographic lens. The piezoactuators with self-locking will be better; otherwise, displacement sensors must be used while reassembling the actuators.

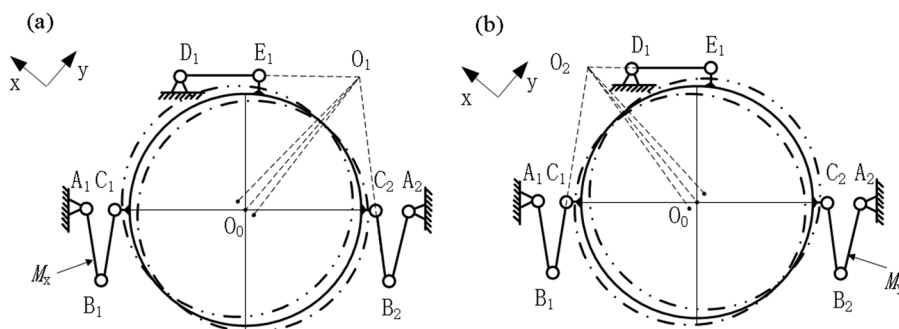


FIG. 1. Movement principle of the XY mechanism: (a) schematic diagram of x -axis movement and (b) schematic diagram of y -axis movement.

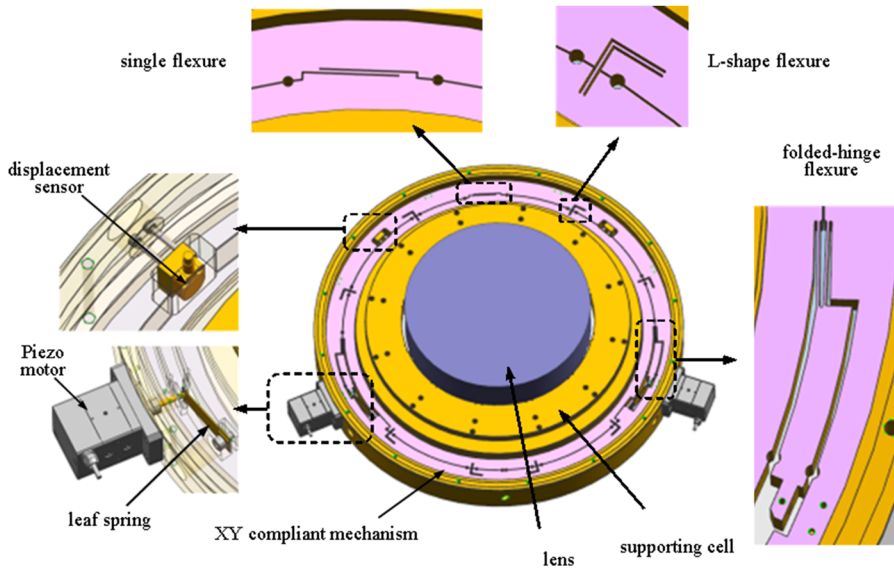


FIG. 2. Schematic diagram of the proposed XY mechanism system.

Figure 3 shows the coordinate system and the structural parameters. The local coordinate system is denoted by x_1 and y_1 , while the overall coordinate system is denoted by x and y , and the origin is the center of the lens O_0 . The structural parameters are defined as follows: the length of $A_1B_1 = A_2B_2 = l_1$, the length of $B_1C_1 = B_2C_2 = l_2$, the length of $D_1E_1 = l_3$, and the length of $O_0C_1 = O_0C_2 = O_0E_1 = r$. The angle between the x_1 axis in the positive direction and A_1B_1 is φ_1 , while the angle between the x_1 axis in the positive direction and A_2B_2 is φ_2 , and the angle between the x_1 axis in the positive direction and D_1E_1 is φ_3 . The angle between A_1B_1 and B_1C_1 is θ_1 , the angle between A_2B_2 and B_2C_2 is θ_2 , the angle between O_0E_1 and the y_1 axis in the negative direction is α , and the angle between the x_1 axis in the positive direction and C_1E_1 is β .

The dimensions of these parameters are listed in Table I.

The relationship between the input displacement of the piezomotor M and the terminal displacement of the lens S is expressed as follows:

$$\Delta S = \begin{bmatrix} \Delta S_x \\ \Delta S_y \end{bmatrix} = J \cdot \Delta M = \begin{pmatrix} j_{11} & j_{12} \\ j_{21} & j_{22} \end{pmatrix} \cdot \begin{bmatrix} \Delta M_x \\ \Delta M_y \end{bmatrix}. \quad (2)$$

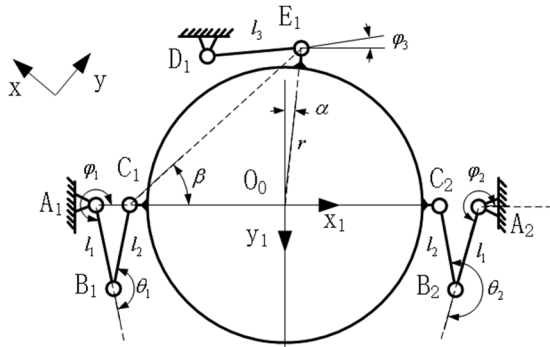


FIG. 3. Coordinate system and structural parameters of the XY mechanism.

Here, J represents the Jacobi motion transmission matrix.

In this paper, the Jacobi matrix of the 1RR-2RRR mechanism is studied algebraically. The procedure used is described as follows:

From its geometrical relationship, the left kinematic chain can be expressed as

$$\overline{A_1O_0} + \overline{O_0C_1} = \overline{A_1B_1} + \overline{B_1C_1}. \quad (3)$$

By taking the derivative of Eq. (3), the velocity vector can then be calculated as

$$\bar{v} + \dot{\beta}(\bar{k} \times \overline{O_0C_1}) = \dot{\varphi}_1(\bar{k} \times \overline{A_1B_1}) + (\dot{\varphi}_1 + \dot{\theta}_1)(\bar{k} \times \overline{B_1C_1}). \quad (4)$$

Here, $\bar{v} = (\dot{x}_1, \dot{y}_1)$ is the lens velocity in the local coordinate system, and \bar{k} is the unit vector of the rotation joint.

Equation (4) can be simplified as follows using the dot product $\overline{B_1C_1}$,

$$\bar{v}_{x1} \cdot \overline{B_1C_1} + \bar{v}_{y1} \cdot \overline{B_1C_1} + \dot{\beta} \bar{k} \cdot (\overline{O_0C_1} \times \overline{B_1C_1}) = \dot{\varphi}_1 \bar{k} \cdot (\overline{A_1B_1} \times \overline{B_1C_1}). \quad (5)$$

TABLE I. Structural parameter dimensions of the XY mechanism.

Parameters	Dimensions
l_1	18.2 mm
l_2	18.2 mm
l_3	22.4 mm
R	156.2 mm
φ_1	271°
φ_2	269°
φ_3	0°
θ_1	178°
θ_2	182°
α	1°

The right kinematic chain can be expressed similarly using the same process,

$$\overline{v_{x1}} \cdot \overline{B_2C_2} + \overline{v_{y1}} \cdot \overline{B_2C_2} + \overline{\beta k} \cdot (\overline{O_0C_2} \times \overline{B_2C_2}) = \overline{\dot{\varphi}_2 k} \cdot (\overline{A_2B_2} \times \overline{B_2C_2}). \quad (6)$$

The top kinematic chain can be expressed as

$$\overline{D_1O_0} = \overline{D_1E_1} + \overline{E_1O_0}. \quad (7)$$

By taking the derivative of Eq. (7), the velocity vector can then be calculated as

$$\overline{v} = \overline{\dot{\varphi}_3} (\overline{k} \times \overline{D_1E_1}) + \overline{\dot{\beta}} (\overline{k} \times \overline{E_1O_0}). \quad (8)$$

Equation (8) can then be simplified as follows using the dot product $\overline{D_1E_1}$:

$$\overline{v_{x1}} \cdot \overline{D_1E_1} + \overline{v_{y1}} \cdot \overline{D_1E_1} = \overline{\dot{\beta} k} (\overline{E_1O_0} \times \overline{D_1E_1}). \quad (9)$$

The dimensions are then inserted into Eqs. (5), (6), and (9) to obtain

$$\begin{cases} \cos 89^\circ \overline{v_{x1}} + \cos 179^\circ \cdot \overline{v_{y1}} + 156.2 \cdot \sin 269^\circ \cdot \overline{\dot{\beta}} = 18.2 \cdot \sin 178^\circ \cdot \overline{\dot{\varphi}_1}, \\ \cos 91^\circ \overline{v_{x1}} + \cos 181^\circ \cdot \overline{v_{y1}} + 156.2 \cdot \sin 91^\circ \cdot \overline{\dot{\beta}} = 18.2 \cdot \sin 182^\circ \cdot \overline{\dot{\varphi}_2}, \\ \overline{v_{x1}} = 156.2 \cdot \sin 91^\circ \cdot \overline{\dot{\beta}}. \end{cases} \quad (10)$$

Formula (10) can be changed into the following matrix format:

$$\begin{bmatrix} -1 + \cos 89^\circ & \cos 179^\circ \\ 1 + \cos 91^\circ & \cos 181^\circ \end{bmatrix} \begin{bmatrix} v_{x1} \\ v_{y1} \end{bmatrix} = \begin{bmatrix} 18.2 \cdot \sin 178^\circ & 0 \\ 0 & 18.2 \cdot \sin 182^\circ \end{bmatrix} \begin{bmatrix} \dot{\varphi}_1 \\ \dot{\varphi}_2 \end{bmatrix}. \quad (11)$$

The relationship between the local coordinate system denoted by x_1, y_1 and the overall coordinate system denoted by x, y can be expressed as

$$\begin{bmatrix} v_x \\ v_y \end{bmatrix} = \begin{bmatrix} -\sin 45^\circ & -\cos 45^\circ \\ \cos 45^\circ & -\sin 45^\circ \end{bmatrix} \begin{bmatrix} v_{x1} \\ v_{y1} \end{bmatrix}. \quad (12)$$

By combining Eqs. (11) and (12), the result can be expressed as

$$\begin{bmatrix} v_x \\ v_y \end{bmatrix} = \begin{bmatrix} 0.4532 & 0.004 \\ -0.004 & -0.4532 \end{bmatrix} \begin{bmatrix} \dot{\varphi}_1 \\ \dot{\varphi}_2 \end{bmatrix}. \quad (13)$$

The relationship between φ_1 and ΔM_x and the relationship between φ_2 and ΔM_y can be expressed as follows:

$$\dot{\varphi}_1 = \Delta M_x / 18.2, \quad (14)$$

$$\dot{\varphi}_2 = -\Delta M_y / 18.2. \quad (15)$$

The positive directions for both ΔM_x and ΔM_y are defined when the actuator pushes the mechanism. When pushing the mechanism forward, φ_2 will increase and φ_2 will decrease, meaning that the signs in formulas (14) and (15) are plus and minus, respectively.

Using Eqs. (13)–(15), the following result can be obtained:

$$\begin{aligned} \begin{bmatrix} \Delta S_x \\ \Delta S_y \end{bmatrix} &= \begin{bmatrix} v_x \\ v_y \end{bmatrix} = \begin{bmatrix} 0.0249 & -2.2 \times 10^{-4} \\ -2.2 \times 10^{-4} & 0.0249 \end{bmatrix} \begin{bmatrix} \Delta M_x \\ \Delta M_y \end{bmatrix} \\ &= J_{THEORY} \cdot \begin{bmatrix} \Delta M_x \\ \Delta M_y \end{bmatrix}. \end{aligned} \quad (16)$$

As shown in Eq. (16), the theoretical Jacobi matrix is a scalar matrix. The ratio of the input displacement to the output displacement is approximately 40:1, so greater lens accuracy can be achieved using scaling processes. In addition, the coupling between x and y is less than 1% and can be controlled to be even lower in practice using a displacement closed loop. The pseudo-rigid-body method uses a rigid joint to replace the flexure joint to calculate the results. The stiffness of the torsional spring and the characteristic radius are not considered, so this method is just used to deduce the relationship approximately at the initial phase. Use of other methods such as finite element method analysis and experiments is also required to verify the mechanism.

The XY mechanism as a sub-house should first ensure the original values of $x/y/z$ /tip/tilt, and then as a movable lens, it can adjust along x/y axis with a high accuracy, small z /tip/tilt coupling errors, and a high rigidity. The original x/y position to the lithography lens axis should be less than 1 μm , z position between adjacent lenses should be less than 1 μm , and tip/tilt to the lithography lens axis should be less than 1 in. The original $x/y/z$ /tip/tilt tolerances can be realized by assembling the lens relative to the sub-house and then glued them together.

The required specifications for the XY compliant mechanism include the range, the accuracy, the coupling rigid motion, and the natural frequency. These parameters are listed in Table II.

The XY mechanism represents a systematic combination of actuators, flexure structures, and capacitive displacement sensors. Each actuator should provide a high resolution, generate a strong force and operate at a high speed, while the sensors should offer both high resolution and high stability. Piezomotors are used as the actuators in this mechanism. In accordance with the XY mechanism requirements, the selected piezomotor has a stroke of 5 mm, a step size that ranges from 10 nm to 7 μm (depending on the controller used), a drive force of 50 N, a holding force of 70 N, and a stiffness in the movement direction of 16 N/ μm . The capacitive displacement sensors are used to provide position feedback. Figure 4 shows a schematic diagram of the displacement sensor and its measurement principle. The principle of capacitive displacement measurement

TABLE II. Required specifications for the XY mechanism.

Parameters	Requirement
Range	$\pm 25 \mu\text{m}$
Accuracy	$\pm 50 \text{ nm}$
Coupling z motion error	$\pm 100 \text{ nm}$
Coupling tip/tilt motion error	$\pm 300 \text{ mas}$
Coupling figure error	rms 2 nm
Natural frequency	200 Hz

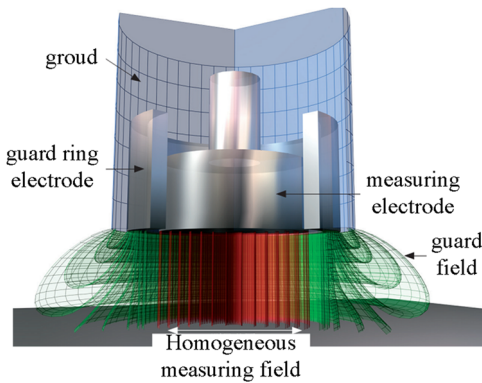


FIG. 4. Measurement principle of the capacitive displacement sensor.

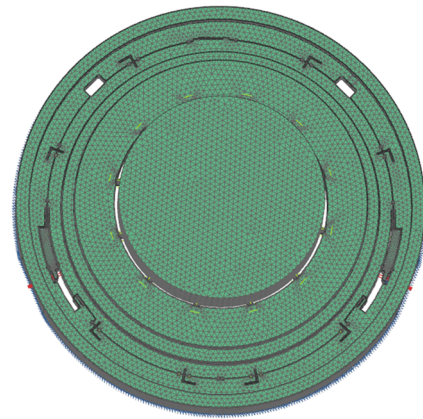


FIG. 5. Finite element model of the XY compliant mechanism.

using a capacitive noncontact displacement transducer (capaNCDT) system is based on operation of an ideal plate-type capacitor. The two electrodes are represented by the sensor itself and the opposing object to be measured. If a constant alternating current flows through the sensing capacitor, then the amplitude of the alternating voltage on the sensor is proportional to the distance between the capacitor electrodes. The main parameters of the capacitive sensor selected here are a measurement range of 200 μm , static resolution (at 2 Hz) of 0.15 nm, a dynamic resolution (at 8.5 kHz) of 4 nm, and a linear accuracy of $\pm 0.2\%$ of the full scale output. The piezomotor and displacement sensor are selected from general products and not customized, so some parameters are excessive.

The XY mechanism control system includes a digital controller, an amplifier module, a piezomotor, and a displacement sensor. The closed-loop controller uses a discrete-time incremental proportional–integral–derivative (PID) control algorithm to guarantee high control accuracy. The feedback displacement is measured using a capacitive position sensor.

IV. FINITE ELEMENT ANALYSIS OF THE XY COMPLIANT MECHANISM

In this section, the Jacobi matrix, the compliance matrix, the travel range, the coupling motion error, the coupling figure error, and the resonance frequency are obtained via finite element analysis.

Figure 5 shows the finite element model of the XY compliant mechanism. The lens and the supporting cell are glued together through several flexure rods. The supporting cell and the inner ring of the XY mechanism are connected by simply gluing the surfaces together. The outside part of the outer ring of the XY mechanism is fixed, and the input force/enforced displacement is applied perpendicular to the outer linkage of the folded-hinge flexure.

The materials used for the lens, the supporting cell, and the XY compliant mechanism are fused silica, aluminum 2A12 alloy, and Invar, respectively. The coefficient of thermal expansion (CTE) values of the supporting cell and the XY compliant mechanism close to the lens will be better, but aluminum 2A12 offers a better cutting performance; therefore, to guarantee high lens supporting

figure accuracy, the prototype used aluminum 2A12 as the supporting cell material. The main parameters of these materials are listed in Table III.

A. Jacobi matrix analysis

The Jacobi matrix of the XY compliant mechanism relates the input displacements of the piezomotors to the output displacements captured by the capacitive sensors. To obtain the Jacobi matrix, we first set the input M_y to zero and vary M_x from 0.1 mm to 1 mm in steps of 0.1 mm. The corresponding simulation output results, S_x and S_y , are obtained and the average values of j_{11} and j_{21} are calculated. Figure 6(a) shows the movement of the lens when the input M_y is zero and M_x is 1 mm. The input M_x is then set to zero, and M_y is varied from 0.1 mm to 1 mm in steps of 0.1 mm. The corresponding simulation output results, S_x and S_y , are obtained and the average values of j_{12} and j_{22} are calculated. Figure 6(b) illustrates the lens movement when the input M_x is zero and M_y is 1 mm.

The simulated Jacobi matrix is then obtained as

$$J_{FEM} = \begin{pmatrix} 0.025591 & 0.000673 \\ 0.001347 & 0.026264 \end{pmatrix}. \quad (17)$$

The top single flexure is not completely left–right symmetrical, and the simulated Jacobi matrix of the designed mechanism is thus not a perfectly scalar matrix.

TABLE III. Main parameters of fused silica, aluminum 2A12 alloy, and Invar.

Material	Young's modulus (Gpa)	Poisson ratio	Density (kg/m^3)	Yield strength (Mpa)
Fused silica	73	0.17	2205	50
Aluminum 2A12	73.1	0.33	2770	393.7
Invar	141	0.259	8050	414

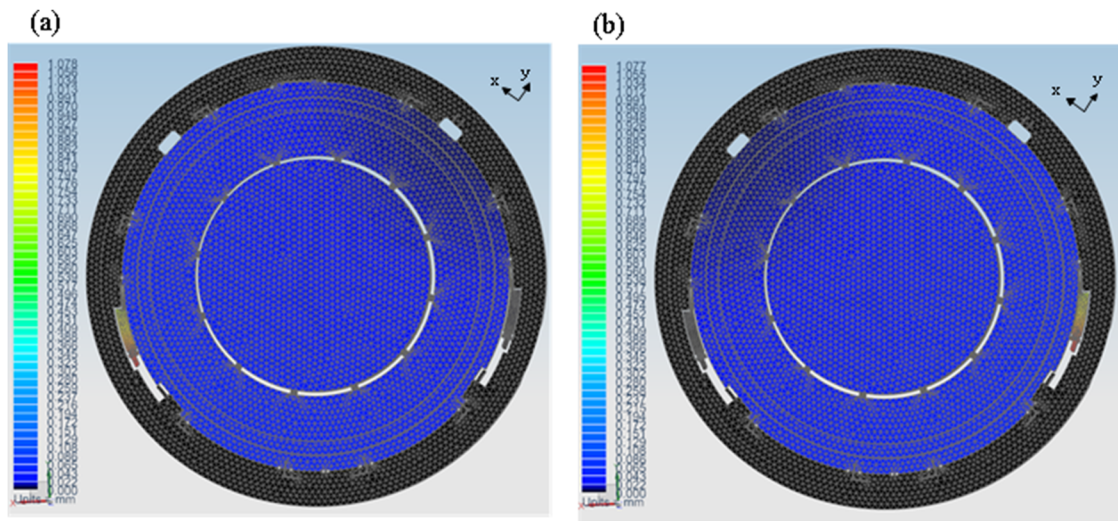


FIG. 6. Kinematic simulations of the XY mechanism: (a) x-axis kinematic simulation and (b) y-axis kinematic simulation.

B. Compliance matrix analysis

The compliance matrix of the XY compliant mechanism relates the input forces F_x and F_y to the output displacements S_x and S_y . Their relationship can be expressed as follows:

$$\Delta S = \begin{bmatrix} \Delta S_x \\ \Delta S_y \end{bmatrix} = C \cdot \Delta F = \begin{pmatrix} c_{11} & c_{12} \\ c_{21} & c_{22} \end{pmatrix} \cdot \begin{bmatrix} \Delta F_x \\ \Delta F_y \end{bmatrix}. \quad (18)$$

Here, C is the compliance matrix.

To obtain the compliance matrix, we must first set the input F_y to zero and then vary F_x from 0.5 N to 2.5 N in steps of 0.5 N. The corresponding simulated output results for S_x and S_y are obtained,

and the average values of c_{11} and c_{21} are then calculated. Figure 7(a) shows the lens movement that occurs when the input F_y is zero and F_x is 2.5 N. The input F_x is then set to zero, while F_y is varied from 0.5 N to 2.5 N in steps of 0.5 N. The corresponding simulated output results for S_x and S_y are obtained, and the average values of c_{12} and c_{22} are then calculated. Figure 7(b) shows the lens movement that occurs when the input F_x is zero and F_y is 2.5 N.

From the simulation results, the simulated compliance matrix is

$$C_{FEM} = \begin{pmatrix} 0.011469 & -2.9 \times 10^{-5} \\ -7.7 \times 10^{-6} & 0.011544 \end{pmatrix}. \quad (19)$$

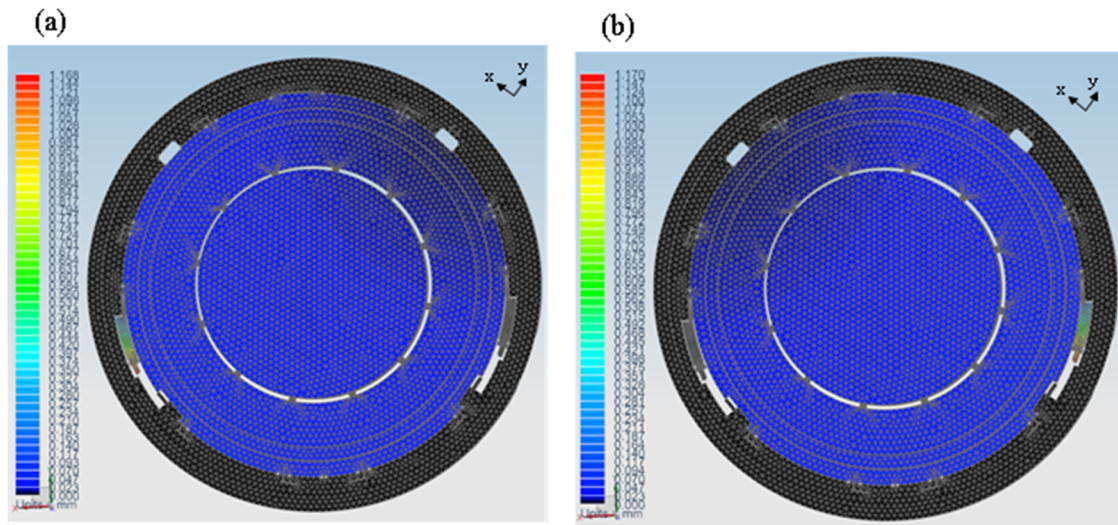


FIG. 7. Compliance matrix simulations of the XY mechanism: (a) x-axis compliance matrix simulation and (b) y-axis compliance matrix simulation.

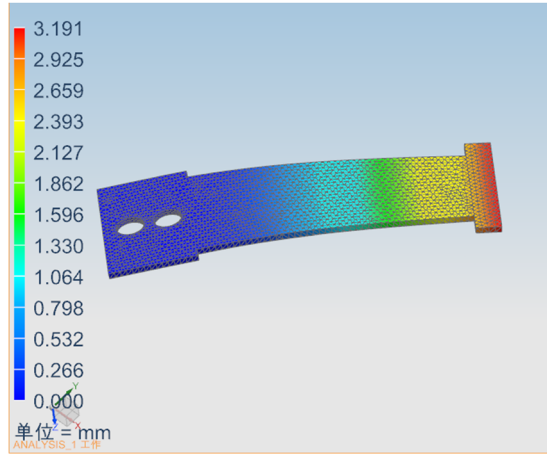


FIG. 8. Nonlinear analysis of the leaf spring.

The simulated compliance matrix gives the relationship between the input forces and the output displacements. This relationship can be expressed as follows:

$$\Delta F = \begin{bmatrix} \Delta F_x \\ \Delta F_y \end{bmatrix} = C_{FEM}^{-1} \Delta S = C_{FEM}^{-1} \begin{bmatrix} \Delta S_x \\ \Delta S_y \end{bmatrix} = \begin{pmatrix} 87.1917 & 0.2190 \\ 0.0582 & 86.6252 \end{pmatrix} \cdot \begin{bmatrix} \Delta S_x \\ \Delta S_y \end{bmatrix}. \quad (20)$$

In practice, a leaf spring is applied to the linkage such that it acts in the direction opposite to that of the piezomotor, and the initial preloading force must also be considered. Figure 8 shows the structure and analysis result of the leaf spring. The two holes are used to fix the spring. The leaf spring stiffness can be obtained through simulations. To attain high stability, a large initial deformation of approximately 3 mm is added to the leaf spring, and the corresponding leaf spring preload force F_{spring_p} is 15.35 N.

When the mechanism operates, the leaf spring deformation change ΔL is equal to the change in the displacement of the

piezomotor ΔM . Therefore, when the displacements ΔS_x and ΔS_y of the mechanism are measured, the leaf spring deformations ΔL_x and ΔL_y can be calculated using Eq. (2) and the simulated Jacobi matrix given as Eq. (17). Therefore,

$$\Delta L = \Delta M = \begin{bmatrix} \Delta M_x \\ \Delta M_y \end{bmatrix} = J_{FEM}^{-1} \cdot \Delta S = \begin{pmatrix} 39.129 & -1.0027 \\ -2.0068 & 38.1264 \end{pmatrix} \cdot \begin{bmatrix} \Delta S_x \\ \Delta S_y \end{bmatrix}. \quad (21)$$

The force that is generated by the leaf spring deformation change can then be obtained as

$$\Delta F_{spring_L} = K \Delta L = \begin{pmatrix} 193.6886 & -4.9632 \\ -9.9337 & 183.7255 \end{pmatrix} \cdot \begin{bmatrix} \Delta S_x \\ \Delta S_y \end{bmatrix}. \quad (22)$$

The final required actuator force is equal to the sum of the mechanism's input force, the spring preload force, and the spring deformation-changed force. The entire force can thus be expressed as follows:

$$\begin{bmatrix} F_{x_actuator} \\ F_{y_actuator} \end{bmatrix} = \begin{bmatrix} \Delta F_x \\ \Delta F_y \end{bmatrix} + F_{spring_p} + \Delta F_{spring_L} = \begin{bmatrix} 15.35 \\ 15.35 \end{bmatrix} + \begin{pmatrix} 280.8803 & -4.7441 \\ -9.8755 & 275.3507 \end{pmatrix} \cdot \begin{bmatrix} \Delta S_x \\ \Delta S_y \end{bmatrix}. \quad (23)$$

Therefore, when the required S_x and S_y both have values of +0.025 mm, the input forces $F_{x_actuator}$ and $F_{y_actuator}$ are 22.25 N and 21.99 N, respectively. In addition, when the required S_x and S_y both have values of -0.025 mm, the input forces $F_{x_actuator}$ and $F_{y_actuator}$ are 8.45 N and 8.71 N, respectively. These forces are used to guide the selection of the piezomotor and to guarantee high mechanism stability.

C. Range, coupling motion errors, and induced figure errors

The range of the proposed mechanism is dependent not only on the piezomotor's input force/displacement but also on the stiffness and strength of the system. Figure 9 shows the maximum element stress when the x -axis range is +25 μm and the y -axis range is +25 μm . The maximum stress in the XY mechanism is 37.7 MPa,

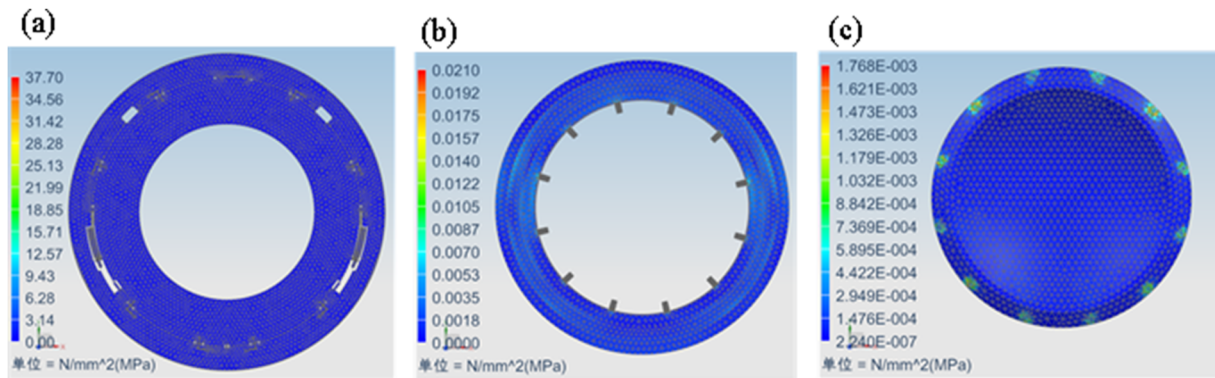


FIG. 9. Stress in the XY mechanism system when the x -axis range is +25 μm and the y -axis range is +25 μm : (a) stress in the XY mechanism; (b) stress in the supporting cell; and (c) stress in the lens.

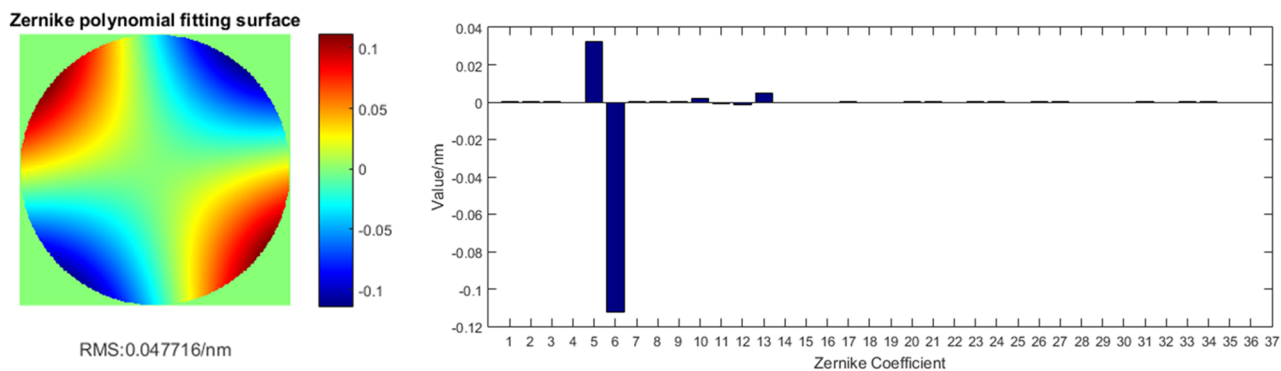


FIG. 10. Figure error and 37 Zernike coefficients for $+25 \mu\text{m}$ movement along the x -axis.

and its weakest area is the folded-hinge flexure area. The maximum stress in the supporting cell is 0.021 MPa, and its weakest area is the area that is in contact with the lens. The maximum stress in the lens is about 0.002 MPa, and its weakest area is the area that is in contact with the cell. When compared with the allowed tensile strengths of 414 MPa for Invar, 393.7 MPa for aluminum 2A12, and 50 MPa for fused silica, the safety factor is high. Therefore, both the x -axis and y -axis ranges of the mechanism exceed $\pm 25 \mu\text{m}$.

When the piezomotors actuate the mechanism, they will induce residual stress transferred to both the supporting cell and the lens, thus inducing a figure error and an out-of-plane rigid motion in the lens. The simulation results show that when the mechanism moves by $+25 \mu\text{m}$ along the x -axis, the induced out-of-plane z /tip/tilt rigid motions are 3.4 nm/6.8 mas/4.9 mas, respectively. The induced figure error and 37 Zernike coefficients are shown in Fig. 10. The root-mean-square (rms) figure error is approximately 0.048 nm, and the main Zernike coefficients are the astigmatisms Z5 and Z6. When the mechanism moves by $+25 \mu\text{m}$ along the y -axis, the induced out-of-plane z /tip/tilt rigid motions are 3.3 nm/4.7 mas/9.4 mas, respectively. The corresponding induced figure error and the 37 Zernike coefficients are shown in Fig. 11. The rms figure error is approximately 0.051 nm in this case, and the main Zernike coefficients are again astigmatisms Z5 and Z6.

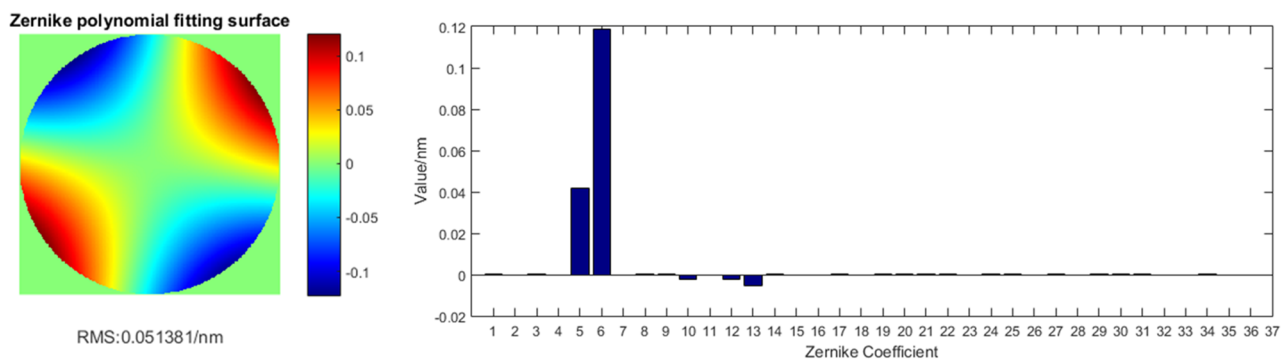


FIG. 11. Figure error and 37 Zernike coefficients for $+25 \mu\text{m}$ movement along the y -axis.

D. Modal analysis

The natural frequencies of the XY mechanism are simulated using modal analysis. Figure 12 shows the first six vibration modes of the proposed mechanism. The modal shape is dependent on not only the XY mechanism but also the supporting cell. The first six natural frequencies, which correspond to the first six vibration modes, are 212 Hz, 245 Hz, 270 Hz, 305 Hz, 426 Hz, and 471 Hz.

E. Analysis of the effects of the L-shaped flexures

In principle, the mechanism is supported by only three points (E1, C1, and C2). However, given that these three points are not evenly distributed, more points (i.e., the L-shaped flexures) are required in practice to balance the weight of the mechanism. Each L-shaped flexure consists of two parts that are perpendicular to each other. One part points toward the lens center and can provide tangential flexibility. The second part, which is arranged tangentially to the lens, can provide radial flexibility. Therefore, each L-shaped flexure provides both tangential and radial flexibilities. The layout of these L-shaped flexures along the circumference can be determined according to stiffness of the supporting points. Figure 13 shows the displacement when the effect of gravity is added. Figure 13(a) shows the displacement of the mechanism without the L-shaped flexures, and the gravity-induced $x/y/z$ /tip/tilt rigid motions are

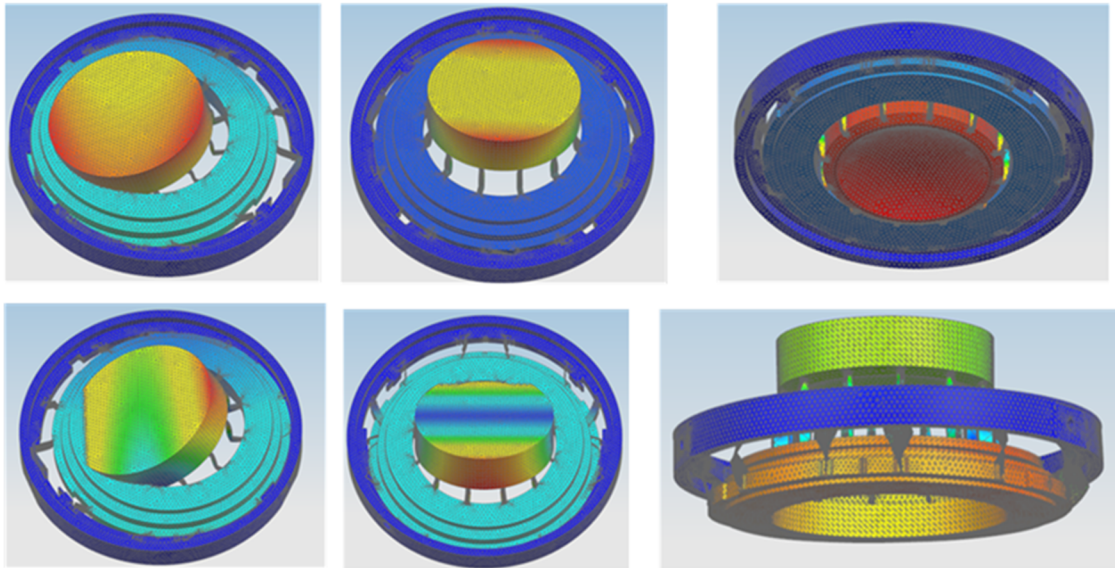


FIG. 12. First six mode shapes of the XY compliant mechanism.

0.304 μm /4 μm /12.6 μm /12.6''/0.9'', respectively. Figure 13(b) shows the displacement of the mechanism with the L-shaped flexures, and the gravity-induced $x/y/z$ /tip/tilt rigid motions are 28 nm/35 nm/4.6 μm /0.1''/0.08'', respectively. The results show that the L-shaped flexures can reduce the x , y , and tip and tilt motions quite obviously, thus demonstrating that the mechanism has a good gravity balancing capability.

The simulated Jacobi matrix and the compliance matrix of the mechanism without the L-shaped flexures are as follows:

$$J_{FEM_withoutL} = \begin{pmatrix} 0.024911 & 0.000930 \\ 0.001896 & 0.026166 \end{pmatrix},$$

$$C_{FEM_withoutL} = \begin{pmatrix} 0.01704 & -8.2 \times 10^{-5} \\ -1.3 \times 10^{-5} & 0.017984 \end{pmatrix}.$$

When compared with the corresponding matrices for the mechanism with the L-shaped flexures, the Jacobi matrix is nearly

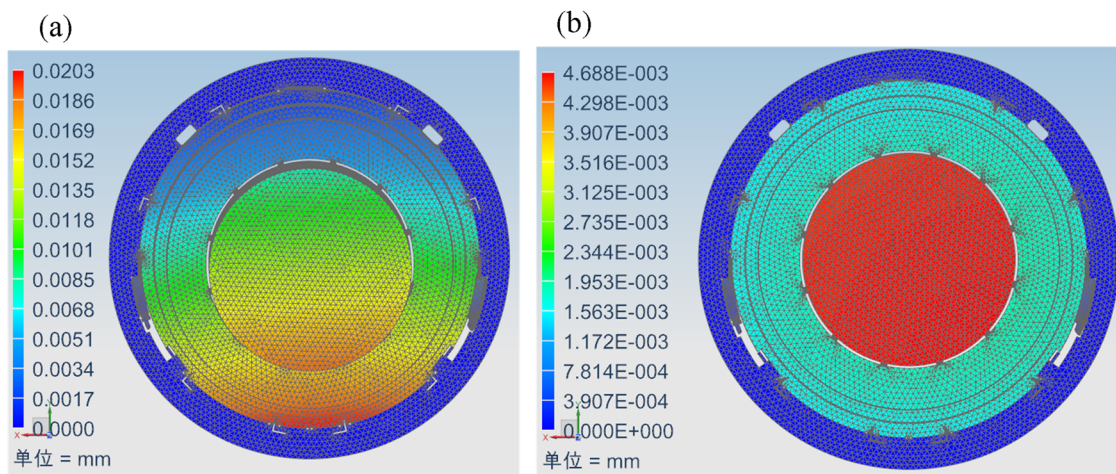


FIG. 13. Displacement of mechanism when the effect of gravity is added: (a) displacement of mechanism without L-shaped flexures and (b) displacement of mechanism with L-shaped flexures.

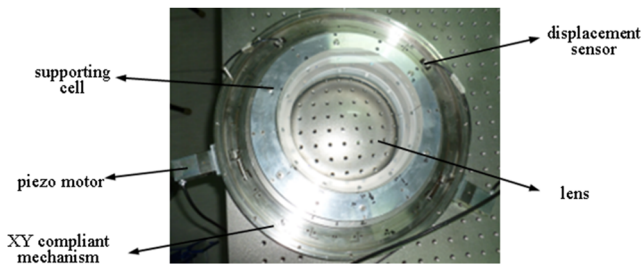


FIG. 14. Prototype XY compliant mechanism.

the same, but the compliance matrix is different. Hence, when L-shaped flexures are added to balance the weight, a larger input force will be required to actuate the mechanism.

V. EXPERIMENTS ON THE XY COMPLIANT MECHANISM

In this section, the real Jacobi matrix, the accuracy, and the out-of-plane coupling rigid motion are obtained on an experimental platform. Figure 14 shows a prototype of the proposed XY compliant mechanism.

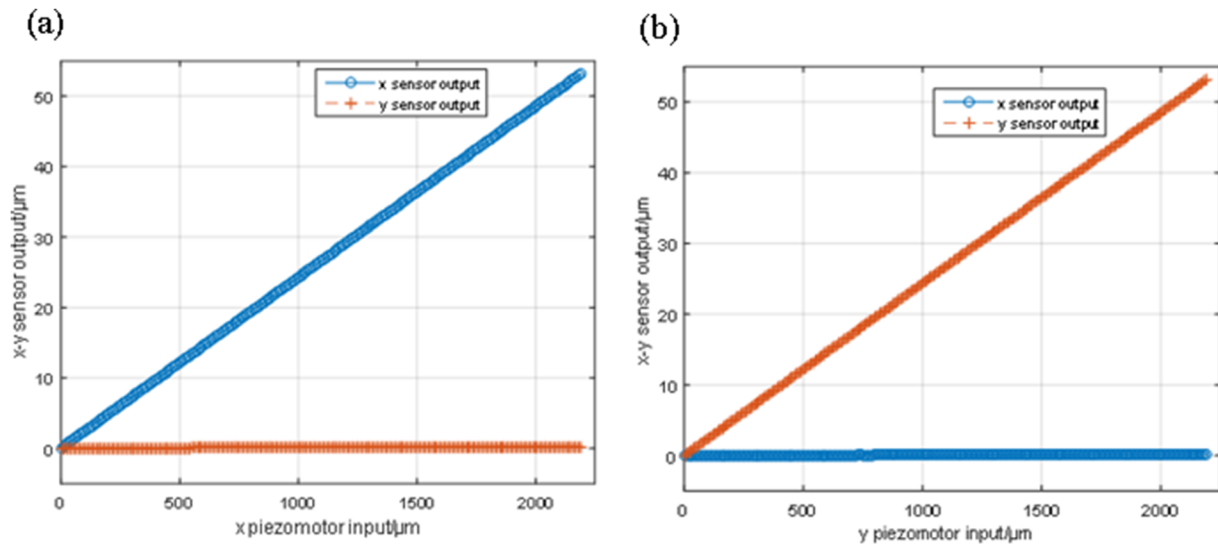


FIG. 15. Relationship between x/y sensor output displacement and piezomotor input displacement: (a) x and y sensor output displacements when the x-axis piezomotor moves and (b) x and y sensor output displacements when the y-axis piezomotor moves.

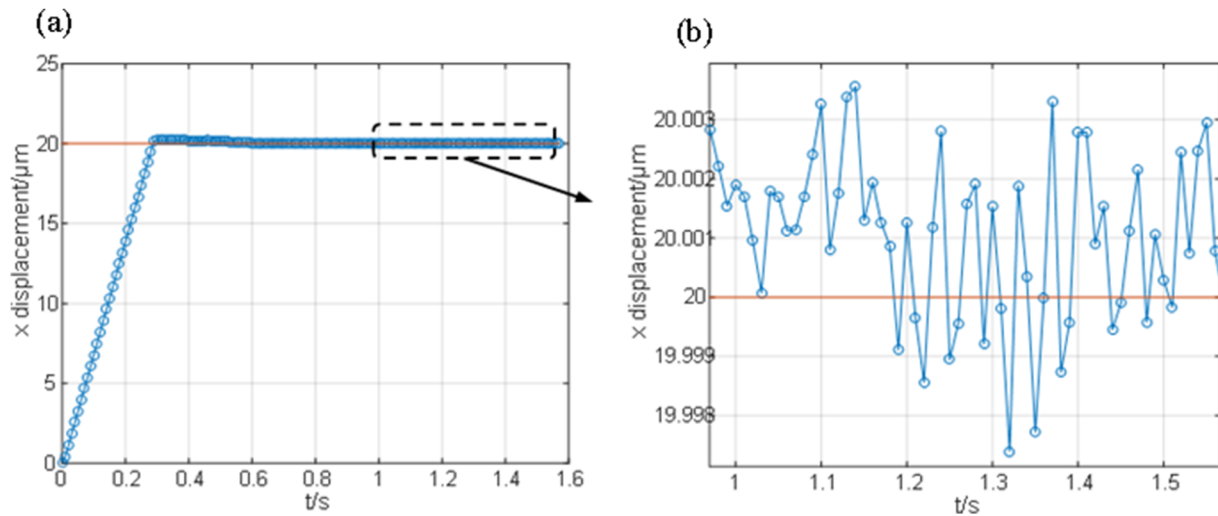


FIG. 16. Dynamic response of XY mechanism when the x displacement is 20 μm : (a) dynamic response and (b) stability of the mechanism when the x displacement is 20 μm .

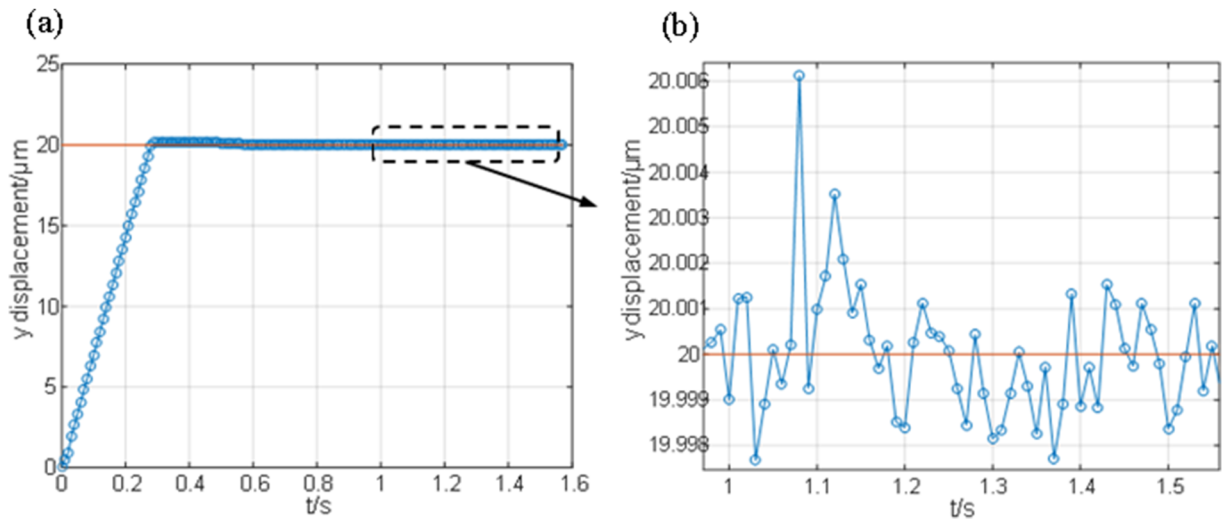


FIG. 17. Dynamic response of XY mechanism when the y displacement is $20\ \mu\text{m}$: (a) dynamic response and (b) stability of the mechanism when the y displacement is $20\ \mu\text{m}$.

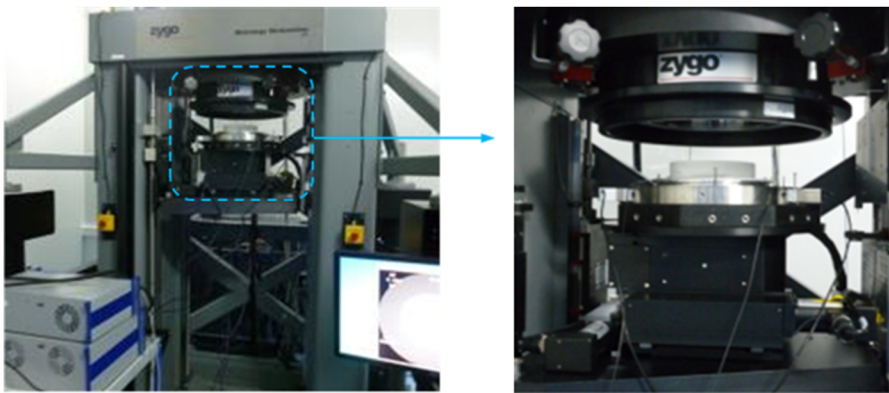


FIG. 18. Photographs of the tip and tilt rigid motions measurement platform.

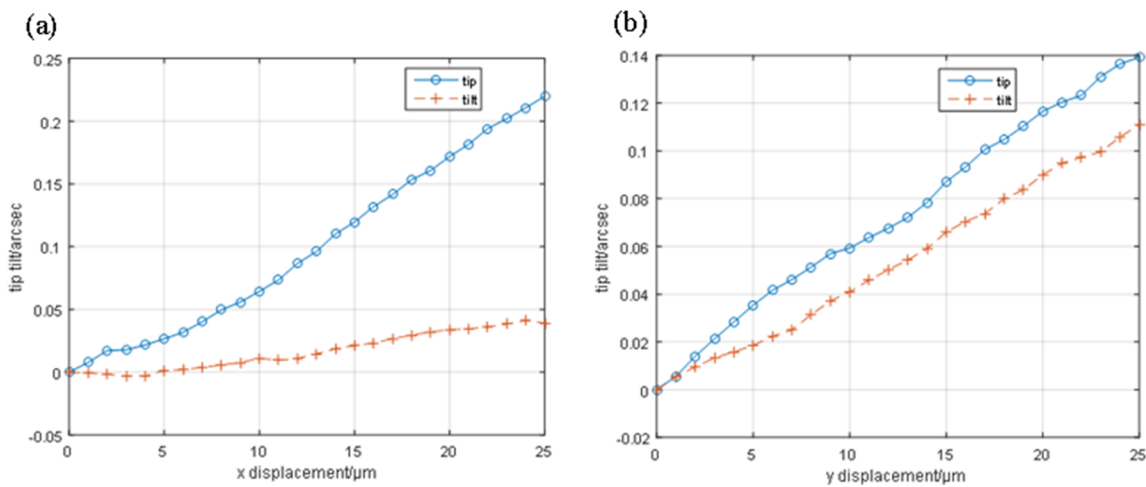


FIG. 19. Induced tip and tilt rigid motion errors of the proposed mechanism: (a) tip and tilt rigid motion errors when the x -axis displacement ranges from $0\ \mu\text{m}$ to $25\ \mu\text{m}$ and (b) tip and tilt rigid motion errors when the y -axis displacement ranges from $0\ \mu\text{m}$ to $25\ \mu\text{m}$.

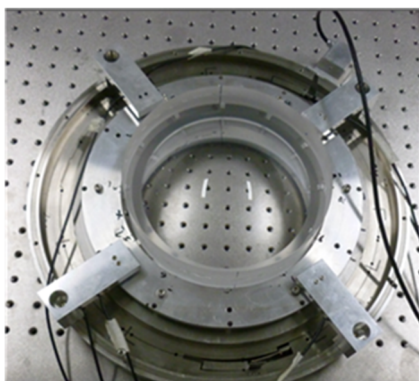


FIG. 20. Photograph of the z rigid motion test equipment.

A. Experiments on the Jacobi matrix

The experimental Jacobi matrix is obtained using an open-loop displacement control system. The procedure described here is based on Eq. (2). First, the input M_y is set at zero, and then, M_x is varied from -1.1 mm to 1.1 mm in steps of 0.01 mm. The corresponding x and y sensor measurement results, which are represented by S_x and S_y , respectively, are then obtained, and the average experimental values of j_{11} and j_{21} are calculated. Using the same method, j_{12} and j_{22} are also calculated. Figure 15(a) shows the x and y sensor output displacements when the x -axis piezomotor input ranges from -1.1 mm to 1.1 mm. The experimental j_{11} and j_{21} values are $0.024 17$ and 2.216×10^{-4} , respectively. Figure 15(b) shows the x and y sensor output displacements when the y -axis piezomotor input ranges from -1.1 mm to 1.1 mm. The experimental j_{12} and j_{22} values are 1.756×10^{-4} and $0.024 29$, respectively. The experimental Jacobi matrix can thus be expressed as

$$J_{REAL} = \begin{pmatrix} 0.024 17 & 1.756 \times 10^{-4} \\ 2.216 \times 10^{-4} & 0.024 29 \end{pmatrix}. \quad (24)$$

Both real factors j_{11} and j_{22} are close to the corresponding values in the theoretical Jacobi matrix given in Eq. (16), with relative errors of 3% and 2.5%, respectively. Simultaneously, they are also close to the corresponding values in the simulated Jacobi matrix given in Eq. (17), with relative errors of 5.9% and 8.1%, respectively. Both j_{12} and j_{21} were small in the simulations, while the actual experimental data are even smaller. The experimental Jacobi matrix indicates that the x -axis coupling error caused by y -axis movement and the y -axis coupling error caused by x -axis movement are 0.91% and 0.72%, respectively.

B. Experiment on accuracy

Figures 16 and 17 show the dynamic responses of the XY mechanism to the specific desired steps. The step displacement is $20 \mu\text{m}$. The data are captured using the capacitive displacement sensor at a sampling rate of 100 Hz. Figure 16 shows the dynamic response when the x displacement is $20 \mu\text{m}$. These results show an accuracy of better than ± 4 nm. Figure 17 shows the dynamic response when the y displacement is $20 \mu\text{m}$. The results in this case show an accuracy of better than ± 7 nm.

C. Experiment on out-of-plane rigid motion errors

The upper surface of the lens used in the mechanism is planar, and the tip and tilt rigid motions can thus be measured using a Fizeau interferometer with a planar etalon, as shown in Fig. 18. During the measurement process, the auto-adjustment function of the interferometer is turned off.

Figure 19(a) shows the tip and tilt rigid motion errors that are induced when the mechanism moves from $0 \mu\text{m}$ to $25 \mu\text{m}$ (in steps of $1 \mu\text{m}$) along the x -axis. The figure shows that the maximum tip is less

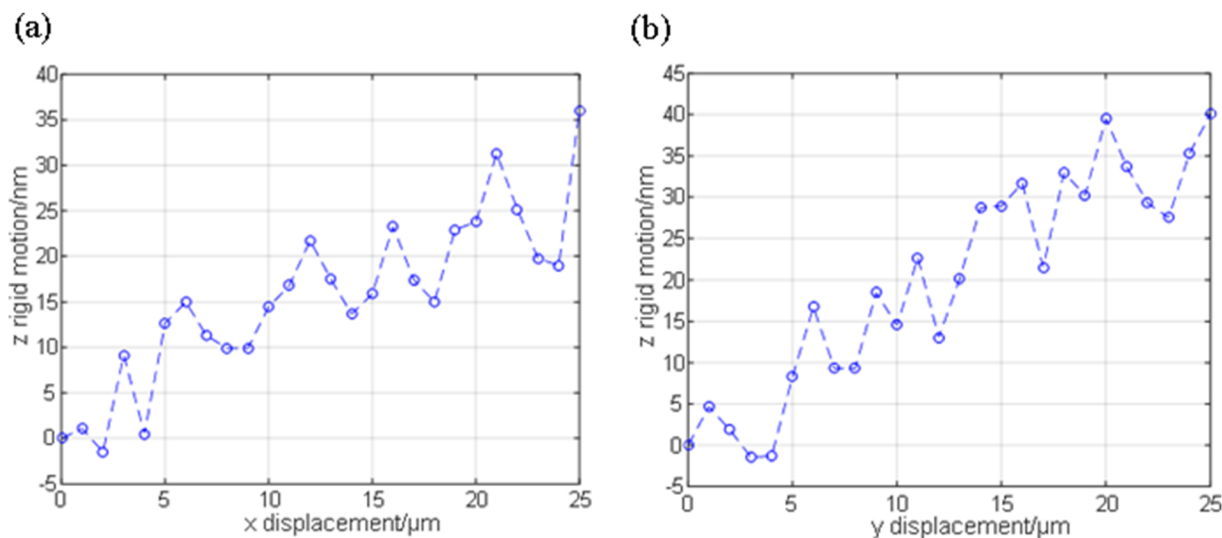


FIG. 21. Induced z rigid motion when the mechanism moves: (a) z rigid motion error when the x -axis displacement ranges from $0 \mu\text{m}$ to $25 \mu\text{m}$ and (b) z rigid motion error when the y -axis displacement ranges from $0 \mu\text{m}$ to $25 \mu\text{m}$.

than 0.22 arc sec and the maximum tilt is less than 0.04 arc sec when the x -axis displacement is 25 μm . Figure 19(b) shows the induced tip and tilt rigid motion errors when the mechanism moves from 0 μm to 25 μm (in steps of 1 μm) along the y -axis. In this case, the maximum tip is less than 0.14 arc sec, and the maximum tilt is less than 0.12 arc sec when the y -axis displacement is 25 μm .

To obtain the z coupling rigid motion of the lens, the z rigid motion of the inner ring is measured instead. Figure 20 shows a photograph of the z rigid motion test equipment. The capacitive displacement sensors are fixed on the outer ring using a sensor holding tool, with the sensors facing the inner ring of the mechanism, which means that the inner ring's movement along the z -axis can then be measured.

The z displacement of the inner ring can be calculated based on the displacements captured by the four sensors. Figure 21 shows the induced z rigid motion when the mechanism moves along the x -axis and when it moves along the y -axis. The maximum z rigid motion is less than 45 nm when the x -axis displacement is 25 μm and is less than 50 nm when the y -axis displacement is 25 μm .

VI. CONCLUSIONS

This paper has presented the design, analysis, and experimental results for a high-precision XY planar compensator for a lithography lens. The XY adjustment mechanism is a monolithic structure composed of an inner ring and an outer ring, which are connected using a top single flexure, left and right folded-hinge flexures, and several L-shaped flexures. The working principle based on the mechanism's 1RR-2RRR configuration was studied, and the theoretical Jacobi matrix of the compliant mechanism was deduced.

The mechanism was simulated using the finite element method. The traveling strokes on both the x -axis and the y -axis exceeded $\pm 25 \mu\text{m}$. The first six natural frequencies of the mechanism were 212 Hz, 245 Hz, 270 Hz, 305 Hz, 426 Hz, and 471 Hz. Experiments were also performed on the XY mechanism. The x -axis and y -axis coupling errors were 0.91% and 0.72%, respectively. The coupling can be controlled to be even weaker through use of a closed-loop controller. The mechanism's closed-loop accuracy was better than $\pm 4 \text{ nm}$ when the x displacement was 20 μm and better than $\pm 7 \text{ nm}$ when the y displacement was 20 μm . The tip/tilt rigid motions were less than 0.22 arc sec/0.04 arc sec when the x -axis displacement was 25 μm and 0.14 arc sec/0.12 arc sec when the y -axis displacement was 25 μm . The z rigid motion was less than 45 nm when the x -axis displacement was 25 μm and was 50 nm when the y -axis displacement was 25 μm .

The results from the simulations and experiments showed that the designed mechanism offers a high accuracy, small coupling rigid motion errors and figure errors, and a high natural frequency. These results validated the proposed design of the XY compliant mechanism. The mechanism can thus be used as a practical compensator in lithography lens applications.

The experimental rigid motion error results are larger than the corresponding results from the simulations, and future work is thus required to analyze the effects of the fabrication and assembly errors. Continuous research is also needed to improve the measurement accuracy and control the coupling errors. As an example, we intend to apply a Fizeau interferometer to measure the power of the lens' lower spherical surface and improve the z -axis rigid motion measurement accuracy.

ACKNOWLEDGMENTS

This work was supported by the National Youth Foundation of China (Grant No. 61504142). The authors are also grateful to the Changchun Institute of Optics, Fine Mechanics, and Physics for the use of their equipment.

REFERENCES

- 1 N. Lobontiu, *Compliant Mechanisms: Design of Flexure Hinges* (CNC Press, Boca Raton, 2003).
- 2 J. W. Ryu, D.-G. Gweon, and K. S. Moon, "Optimal design of a flexure hinge based XY ϕ wafer stage," *Precis. Eng.* **21**, 18–28 (1997).
- 3 Y. K. Yong and T.-F. Lu, "Kinestatic modeling of 3-RRR compliant micro-motion stages with flexure hinges," *Mech. Mach. Theory* **44**, 1156–1175 (2009).
- 4 S. Polit and J. Dong, "Development of a high-bandwidth XY nanopositioning stage for high-rate micro-/nanomanufacturing," *IEEE/ASME Trans. Mechatron.* **16**, 724–733 (2011).
- 5 Y. Li and Q. Xu, "A novel piezoactuated XY stage with parallel, decoupled, and stacked flexure structure for micro-/nanopositioning," *IEEE Trans. Ind. Electron.* **58**, 3601–3615 (2011).
- 6 H.-S. Kim, E.-J. Kim, and B.-S. Song, "Diamond turning of large off-axis aspheric mirrors using a fast tool servo with on-machine measurement," *J. Mater. Process. Technol.* **146**, 349–355 (2004).
- 7 S. Rakuff and J. F. Cuttino, "Design and testing of a long-range, precision fast tool servo system for diamond turning," *Precis. Eng.* **33**, 18–25 (2009).
- 8 Z. Zhu, X. Zhou, Z. Liu, R. Wang, and L. Zhu, "Development of a piezoelectrically actuated two-degree-of-freedom fast tool servo with decoupled motions for micro-/nanomachining," *Precis. Eng.* **38**, 809–820 (2014).
- 9 Y.-T. Liu and B.-J. Li, "A 3-axis precision positioning device using PZT actuators with low interference motions," *Precis. Eng.* **46**, 118–128 (2016).
- 10 A. S. Gaunekar, G. P. Widdowson, N. Srikanth, and W. Guangneng, "Design and development of a high precision lens focusing mechanism using flexure bearings," *Precis. Eng.* **29**, 81–85 (2005).
- 11 B. Wang, X. Chen, M. Zhu, R. Su, Z. Huang, and X. Fu, "Analysis of a tripod flexure mechanism (TFM) for mirror sub-assemblies," *Fusion Eng. Des.* **129**, 277–285 (2018).
- 12 K. Guo, M. Y. Ni, H. N. Chen, and Y. X. Sui, "A monolithic adjusting mechanism for optical element based on modified 6-PSS parallel mechanism," *Sens. Actuators, A* **251**, 1–9 (2013).
- 13 L. C. Hale, *Principles and Techniques for Designing Precision Machines* (University of California, California, 1999).
- 14 Y. Lu, D. Fan, and Z. Zhang, "Theoretical and experimental determination of bandwidth for a two-axis faststeering mirror," *Optik* **124**, 2443–2449 (2013).
- 15 P.-Z. Li, X.-D. Wang, Y.-X. Sui, D.-F. Zhang, D.-F. Wang, L.-J. Dong, and M.-Y. Ni, "Piezoelectric actuated phase shifter based on external laser interferometer: Design, control and experimental validation," *Sensors* **17**, 838 (2017).
- 16 T. J. Teo, G. Yang, and I.-M. Chen, "A large deflection and high payload flexure-based parallel manipulator for UV nanoimprint lithography: Part I. Modeling and analyses," *Precis. Eng.* **38**, 861–871 (2014).
- 17 B. Hoeflinger, *CHIPS 2020 Volume 2: New Vistas in Nanoelectronics* (Springer, Heidelberg, 2016).
- 18 T. Matsuyama, Y. Ohmura, and D. M. Williamson, "The lithographic lens: Its history and evolution," *Proc. SPIE* **6154**, 615403 (2006).
- 19 C. Yao and Y. Gong, "Simulation research on the thermal effects in dipolar illuminated lithography," *J. Opt. Soc. Korea* **20**, 251–256 (2016).
- 20 Y. Ohmura, Y. Tsuge, T. Hirayama, H. Ikezawa, D. Inoue *et al.*, "High-order aberration control during exposure for leading-edge lithography projection optics," *Proc. SPIE* **9780**, 97800Y (2016).
- 21 Y. Yoda, A. Hayakawa, S. Ishiyama, Y. Ohmura, I. Fujimoto *et al.*, "Next-generation immersion scanner optimizing on-product performance for 7nm node," *Proc. SPIE* **9780**, 978012 (2016).